Available online at www.sciencedirect.com
ScienceDirect
Journal of Sound and Vibration 301 (2007) 74–92
JOURNAL OF SOUND AND VIBRATION
www.elsevier.com/locate/jsvi

The dynamics and acoustics of viscous two-dimensional leapfrogging vortices

Jeff D. Eldredge

Mechanical and Aerospace Engineering, University of California, Los Angeles, CA 90095, USA

Received 17 June 2005; received in revised form 1 September 2006; accepted 5 September 2006
Available online 9 November 2006

Abstract

The dynamics and acoustics of two identical pairs of counter-rotating vortices in viscous compressible flow are investigated. Each finite-sized vortex has an initially Gaussian distribution of vorticity. The dilating vortex particle method—developed in previous work—is used for the high-fidelity solution of the full compressible Navier–Stokes equations in the nearfield and a portion of the acoustic field; the radiated sound is extrapolated from a Kirchhoff surface adjusted for mean flow. The trailing vortex pair periodically slips through the leading pair, producing a sharp acoustic pulse. During the ensuing relaxation period as the cores return to horizontal alignment, filaments of vorticity are stripped from the outer part of each vortex while its inner core remains intact, and a small oscillatory acoustic signal is emitted. In contrast to previous studies of inviscid patches of uniform vorticity, this signal is much weaker than the slip-through pulses. Passive particles in the vortex cores are used to explore the filament evolution and core dynamics. The elastic deformation of the inner core, which is a crucial source of sound in previous patch studies, is found to be insignificant to sound production in these smooth cores. Instead, the weak oscillatory component of sound is generated by the anchors of filamentary structures as they rotate about the core. After several slip-through cycles, the pairs coalesce to form a single counter-rotating pair, and the sound emissions become weak and sinusoidal.

1. Introduction

The sound produced by many fluid flows is fundamentally connected with motions and distortions of vorticity. In order to understand the basic sound-generating processes in a more complex flow, it is useful to investigate the acoustics of simple 'building-block' vortical motions. The goal of this work is to use direct numerical simulation (DNS) of the full compressible Navier–Stokes equations to elucidate the acoustic role of specific phenomena that occur in a particular building-block flow—in this case, two-dimensional leapfrogging vortex pairs—and which may be present in more complex flows. The flow chosen here is meant to provide as rich a dynamical behavior as possible, while still retaining a degree of simplicity (e.g. symmetries, absence of influence of external flow, etc.).

E-mail address: eldredge@seas.ucla.edu.

0022-460X/$ - see front matter © 2006 Elsevier Ltd. All rights reserved.
doi:10.1016/j.jsv.2006.09.015

1.1. Vortex sound

The fundamental role of vorticity in aeroacoustics has been explored many times, and only a brief survey of previous work is attempted here. Powell [1] used physical arguments to highlight this role, developing an expression for the far-field sound from the inviscid equations of motion. His was the first work to label the radiated sound from vortical motions as 'vortex sound.' The mathematical formulation was later refined by Howe [2], who arrived at a convected wave equation for the stagnation enthalpy which is exact for inviscid flow. This form contains several 'forcing' terms on the right-hand side, among them $\nabla\cdot(\omega\times u)$. The rigorous justification for treating this and other right-hand side terms as acoustic sources that can be determined a priori has been carefully delineated by several researchers (see, e.g., Ref. [3]) using matched asymptotic expansions between inner and outer flows. Such an argument requires a distinct separation of flow and acoustic length scales, which is generally only possible when the characteristic Mach number is small.

The importance of vorticity in sound generation can therefore be explicitly identified in a low Mach number flow. By expanding the differences in retarded time across an acoustically compact flow region, the pressure fluctuations at an observation point in the far-field can be related to fluctuating vorticity in the nearfield [4,5], and a quadrupolar source is identifiable:

$$p'(x,t)\approx-\frac{\rho_\infty x_i x_j}{12\pi a_\infty^2|x|^3}\frac{\mathrm{d}^3}{\mathrm{d}t^3}\int y_i(\omega\times y)_j(y,t-|x|/a_\infty)\,\mathrm{d}^3y. \tag{1}$$

Thus, the rates of change of the second moments of vorticity are ostensibly important to sound production in unbounded flows. A two-dimensional version of the equation can also be developed, which Mitchell et al. [6] used to predict the sound from co-rotating vortices and compare with a direct computation from compressible DNS. In their critical evaluation of several acoustic analogies, they found that the Möhring formula predicted the radiated sound very well when the source region was sufficiently compact, though the restriction on compactness was stronger than is required by the Powell–Howe analogy.

1.2. Previous investigations of leapfrogging rings and pairs

Because of the relative ease with which Eq. (1) can be applied, analysis of the acoustics of complex low Mach number flows is possible when data from only the nearfield flow are available (e.g. from incompressible simulation or particle image velocimetry measurements; for the latter, see Ref. [7]). Some investigators have adopted a simpler description of the nearfield, through inviscid simulation of uniform patches of vorticity with the method of contour dynamics. Shariff et al. [8] examined the interactions of coaxial vortex rings in leapfrogging (same-sign circulation) configuration, and used the Möhring formula, Eq. (1), to predict the subsequent sound. In the case of thin cores, it was found that, in addition to the sound pulses created by the slipping of one ring through the other, a higher frequency component was produced that was attributed to core deformation. This additional component was stronger than the slip-through sound, and increased the radiated power significantly.

Moreover, the high-frequency sound did not vary in amplitude over time. In order to illustrate the importance of core deformations, they used an elliptical core model developed by Melander et al. [9] and compared the dynamics of this model with the contour dynamics simulation. They found good agreement in their acoustic predictions for the thin-core case, which suggests that rotations and low-order deformations of the core are primarily responsible for this high-frequency sound in vorticity patch dynamics.

The contour dynamics approach has also been used by Tang and Ko [10] to investigate leapfrogging vortex rings [11] and two-dimensional leapfrogging pairs [12]. The Möhring equation, Eq. (1), was decomposed to identify the relative contributions of centroid motion and core deformation in the sound generation process of uniform vorticity patch dynamics. In the three-dimensional case, they identified different types of behavior depending on the thickness and initial separation of the rings. Thin identical rings slipped through one another and deformed, producing an acoustic pattern similar to that found by Shariff et al. [8], though there was a slight modulation in the high frequency sound. Thick identical cores quickly coalesced and formed long filaments that wrapped around the cores. Similarly, in the two-dimensional investigation [12], the

high-frequency component was present and generally dominated the slip-through sound. Moreover, this high-frequency portion persisted without decay between slip-through events, and increased after each slip-through as core deformations became amplified.

The advantage of using contour dynamics is that the vortices and their boundaries are explicitly defined, which allows the Möhring source terms to be easily broken down into contributions from each vortex. However, real fluid effects, such as viscosity and nearfield compressibility, are obviously ignored in this approach, and such effects may have direct or indirect consequences on the acoustics. Non-uniform distributions of vorticity cannot be simulated, and therefore the effect of this non-uniformity on the magnitude of the acoustic field components cannot be assessed.

For these reasons, DNS of the full viscous equations of motion is essential to completely understand the dynamics and acoustics of this flow. Verzicco et al. [13] solved the incompressible Navier–Stokes equations for identical leapfrogging rings using a second-order-accurate finite difference method. Because of their interest in simulating pairing in real round jets, their computations focused on the short-time behavior of rapidly coalescing rings with an initial separation of one ring radius, using a variety of core sizes. They explored the effect of vorticity distribution, using both Gaussian and top-hat profiles; the latter allowed comparison with results of contour dynamics simulations. A key observation was that the acoustic amplitude produced by the coalescing top-hat vortices was significantly larger than for the Gaussian cores. Moderate circulation Reynolds numbers in the range 1000–4000 were used, though little variation in the subsequent acoustic field was observed in this small range.

In contrast to these incompressible simulations, Inoue [14] solved the full compressible Navier–Stokes equations by using a sixth-order-accurate compact finite difference scheme, in order to directly compute the sound produced by leapfrogging vortex rings with Gaussian-distributed cores. Qualitative features of the slip-through sound were similar to those observed in previous studies, but the high-frequency acoustic component was absent, which is likely due to viscous damping at the Reynolds number of 2000 that was used throughout the work. The rings coalesced after approximately three slip-throughs, resulting in much smaller sinusoidal pressure fluctuations.

1.3. Motivation for present work

The primary purpose of the present work is to explore the relative importance to sound production of specific dynamic processes in the vortices when smooth initial distributions of vorticity are subject to real fluid effects. The dynamics and sound produced by viscous two-dimensional leapfrogging vortex pairs—with initially Gaussian vorticity distributions—will be investigated by DNS. A large portion of the effort will be devoted to studying the acoustic effects of vortex core deformation, which are distinguishable because of the relatively large circulation Reynolds number of 10,000 that is used. Furthermore, this study will primarily involve relatively thin cores, for which coalescence only occurs after several slip-through cycles.

This work will rely on high-fidelity DNSs of the full compressible Navier–Stokes equations, using a compressible viscous vortex particle method, developed in previous work [15]. This Lagrangian method relies on convecting computational particles that carry vorticity and dilatation, which allows a more direct analysis of these quantities' roles in producing sound. The nearfield dynamics of the vortex pairs are computed, along with a limited portion of the acoustic field; the external acoustic field is then extrapolated by using a Kirchhoff method. In Section 2, the problem configuration is described, along with relevant physical parameters. The vortex particle method is briefly described in Section 3. The simulation results and their analysis are presented and discussed in Section 4.

2. Problem description

The initial configuration of the vortices is depicted in Fig. 1. Four vortices are arranged at the corners of a rectangle of width $2\delta_{x0}$ and height $2\delta_{y0}$. The configuration is described by a coordinate system with origin at the center of the rectangle and axes parallel to its sides. The two vortices in the upper-half plane are assigned positive (counter-clockwise) circulation Γ, and their respective images in the lower-half plane are given the same circulation of opposite sense.

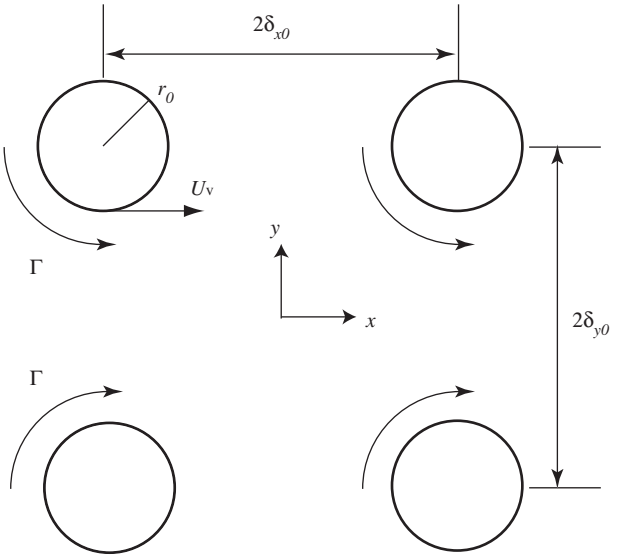

Fig. 1. Initial configuration of vortices.

The antisymmetry of the system about the x-axis ensures that the net circulation vanishes, and the center of vorticity translates in the positive x direction. In the limit of vanishing core sizes (but constant vortex strengths), the resultant system of four point vortices undergoes a periodic leapfrogging motion. The trailing counter-rotating pair slips through the leading pair, thereby reversing their roles and causing the process to repeat. The point vortex motion is completely characterized by the initial aspect ratio, δ_{y0}/δ_{x0}. Throughout these computations, this parameter will have the value unity. A characteristic time scale of the point vortex motion is $T = 8\pi^2\delta_{x0}^2/\Gamma$, which represents the period of full rotation as $\delta_{y0}/\delta_{x0} \to \infty$ (that is, as the cores are well removed from the axis of symmetry). The period and forward propagation speed of the system are classical results [16,17], and are, respectively, given by

$$T_p = \frac{32\pi\delta_{x0}^2/\Gamma}{k^2(1+k)}[E(k) - (1-k^2)K(k)] \tag{2}$$

and

$$\bar{U} = \frac{\delta_{y0}\Gamma}{4\pi\delta_{x0}^2}\left[\frac{k^2E(k)}{E(k) - (1-k^2)K(k)}\right], \tag{3}$$

where K and E are the complete elliptic integrals of the first and second kind, respectively, and $k = (1 + \delta_{y0}^2/\delta_{x0}^2)^{-1}$. Thus, for $\delta_{y0}/\delta_{x0} = 1$, the period is $T_p = 54.46\delta_{x0}^2/\Gamma$ and the mean speed is $\bar{U} = 0.1437\Gamma/\delta_{x0}$.

The radii of cores with finite size provide an additional degree of freedom, r_0/δ_{x0}. Each vortex core has an initially Gaussian distribution of vorticity about its center. Defining the radius r_0 of each vortex to coincide with the distance at which its self-induced velocity is maximum (denoted by U_V), the vorticity is distributed according to

$$\omega = \frac{1.25\Gamma}{\pi r_0^2}\exp(-1.25r^2/r_0^2), \tag{4}$$

where the circulation is given by $\Gamma = 2\pi(0.7)^{-1}U_V r_0$. The core Mach number is defined as $M_V = U_V/a_\infty$. Moderate sized cores translate with a mean speed given approximately by Eq. (3). Thus, the Mach number of mean forward propagation, for $\delta_{y0}/\delta_{x0} = 1$, is $\bar{M} = \bar{U}/a_\infty = 1.290\,M_V r_0/\delta_{x0}$ and the acoustically scaled period of rotation is $a_\infty T_p/\delta_{x0} = 6.067\delta_{x0}/(M_V r_0)$. Throughout these computations, $M_V r_0/\delta_{x0} = 0.084$, so

$\bar{M} = 0.1084$ and $a_\infty T_p/\delta_{x0} = 72.23$. The Reynolds number is based on circulation, and is defined here as $Re_\Gamma = \Gamma/v$. The Prandtl number is 0.7.

3. Numerical solution method

The problem of leapfrogging vortices in viscous compressible flow is solved numerically with high fidelity to the full compressible Navier–Stokes equations, by using the dilating vortex particle method, developed by Eldredge et al. [15]. The reader is referred to this previous work for details (as well as Cottet and Koumoutsakos [18] for background on the incompressible vortex particle method); only the basic premises and the numerical parameters used are described here. The particle-based method focuses on the vorticity and rate of dilatation rather than velocity directly. Eldredge et al. [15] demonstrated the method to be convergent. In this previous work, the solution for the dynamics and acoustics of co-rotating vortices—at Reynolds numbers similar to those investigated in the present work—was shown to agree very closely with the compact finite difference solution of Mitchell et al. [6].

The particle strengths are evolved by integrating the Lagrangian forms of the mass, momentum and energy equations, using conservative particle approximations of the various terms. A fourth-order Runge–Kutta integration scheme with a time step size of $\Delta t = 0.009\delta_{x0}/a_\infty$ is used throughout; results were indistinguishable when this time step size was halved. Spatial derivatives in the equations of motion are approximated by using particle strength exchange [19] with eighth-order-accurate kernels developed by Eldredge et al. [20]. The spatial refinement is chosen so that 25 particles traverse the core diameter of each vortex. When this resolution was doubled, it resulted in a smaller than 0.1% change in the predicted acoustic field. The reader is referred to Ref. [15] for more details on the convergence checking for the similar problem of a co-rotating vortex pair.

A weak—and inconsequential—acoustic transient is emitted by the initial conditions, and the quantities quickly settle to physical values (see Ref. [15] for an example of this transient). The domain of particle coverage is truncated and supplemented with an artificial boundary condition—a first-order radiation condition [21]—and enforced in a buffer zone of four particles depth. Particles are re-initialized to a uniform grid every two time steps to prevent large distortions in the particle distribution from degrading the computation (note that this re-initialization is not a disruption in the computation; it is effectively a re-identification of the field quantities with new local interpolants). This re-initialization relies on a sixth-order-accurate Gaussian kernel to interpolate old particle strengths to new particles.

A uniform flow, U_∞, in the x direction is added to the velocity field to keep the vortex system approximately stationary in the mean; U_∞ is set to the negative of the mean speed of the equivalent point vortex system, $U_\infty = -\bar{U}$, where $\bar{U}$ is determined by Eq. (3). The acoustic field outside the particle coverage is computed with a Kirchhoff surface that accounts for the convection of the vortex system; see Appendix A for details.

4. Results and discussion

In this section, the results of the compressible vortex particle method simulations are presented and thoroughly analyzed. In order to explore the dynamics and acoustics of leapfrogging with greatest clarity, particular attention will be focused on vortex pairs that undergo several leapfrogging cycles before coalescing. Such behavior is exhibited by vortices with core sizes in the range $r_0/\delta_{x0} \approx 0.2$–$0.35$ and at moderate Reynolds number. Throughout these computations, a Reynolds number of 10^4 is used.

An example of the results obtained in this work is presented in Fig. 2, which depicts the vorticity and dilatation fields above the symmetry axis resulting from a simulation with $\delta_{y0}/\delta_{x0} = 1$ and $r_0 = 0.3\,\delta_{x0}$. Several snapshots at regular intervals are shown, beginning with the initial field at $a_\infty t/\delta_{x0} = 0$. Dilatation is initially set to zero, but quickly adjusts to an appropriate level during an initial transient period. At $a_\infty t/\delta_{x0} = 18$, the vortices are vertically aligned during their first slip-through, and the vortex cores are distorted from their original circular configurations. The dilatation in each vortex contains four lobes of alternating sign, which is characteristic of co-rotating vortex pairs [6,15]. The dilatation is much larger in magnitude in the vortex currently slipping through. At $a_\infty t/\delta_{x0} = 36$, the vortices have completed a half-cycle of leapfrogging, and the four-lobed dilatation structures are nearly identical in each vortex. Though the inner core of each vortex is nearly circular, the outer vorticity contours have become stretched and filaments have formed.

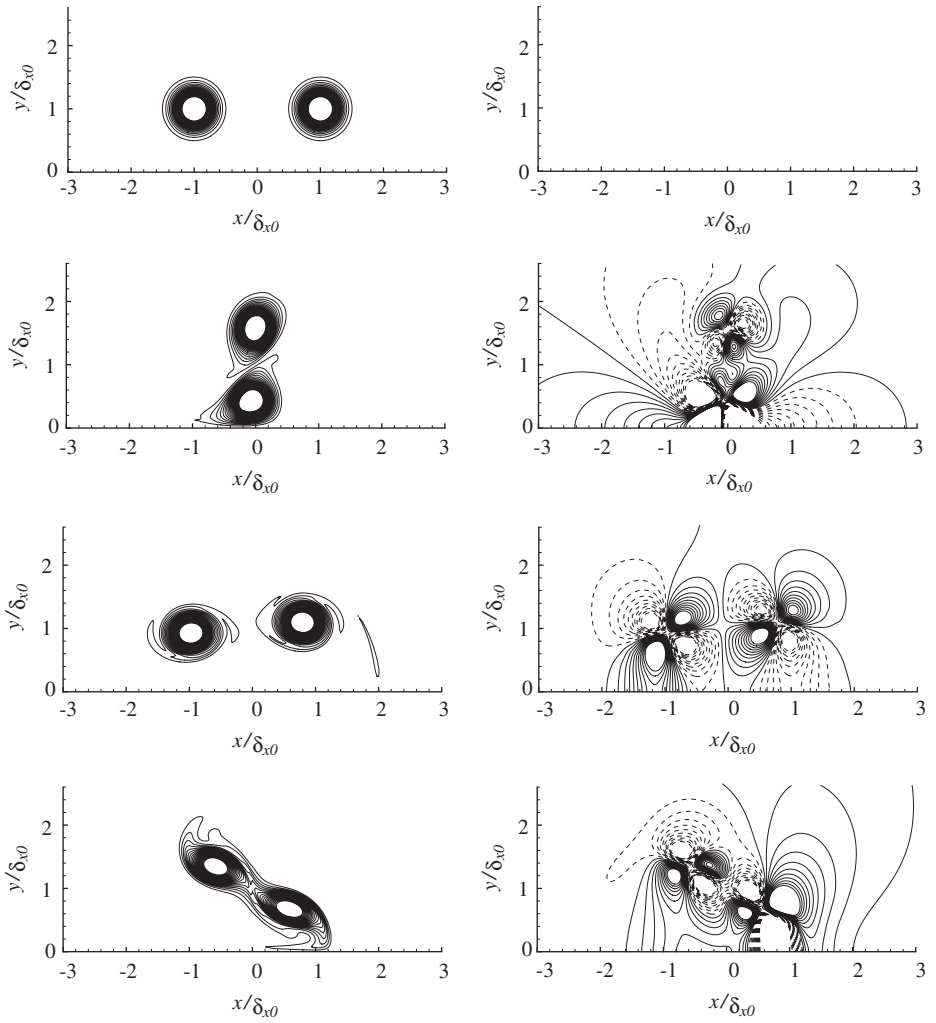

Fig. 2. Vorticity (left) and dilatation (right) for $r_0/\delta_{x0} = 0.3$ at $a_\infty t/\delta_{x0} = 0$, 18, 36 and 54 (from top to bottom). Vorticity contours are in the range [0.1,2] in increments of 0.1; dilatation contours are in [−0.01,0.01] in increments of 0.001. Negative contour levels are depicted with dashed lines. Vorticity and dilatation for $r_0/\delta_{x0} = 0.3$ at $a_\infty t/\delta_{x0} = 72$, 90, 108, and 126 (from top to bottom).

This slip-through process repeats itself two more times, with increasing distortion and filamentation of the vortices. During the fourth slip-through at $a_\infty t/\delta_{x0} \approx 90$, the vortices are stretched across a common interface, and their four-lobed dilatation structures are undergoing a topological change. Their cores are drawn together and coalesce into a single structure, with a new four-lobed dilatation structure, as seen at $a_\infty t/\delta_{x0} = 108$. The individual cores still retain some identity at this instant, but by $a_\infty t/\delta_{x0} = 126$, the cores have diffused together into a single elliptical core. Note that the new counter-rotating vortex pair translates with a smaller velocity than the original pairs, reflected by a rearward drift in the frame of reference.

4.1. Acoustics

Snapshots of the instantaneous pressure field at $a_\infty t/\delta_{x0} = 110$ are depicted in Fig. 3 for two different core sizes, $r_0 = 0.25\delta_{x0}$ and $r_0 = 0.3\delta_{x0}$. For the case of the smaller cores, a crest with four alternating-sign sectors is radiating from the source, followed by another crest of opposite signed sectors; ahead of and behind these crests are substantial regions of relative silence. A notable feature of this field is the fore/aft asymmetry. The wavefronts have an apparent origin that is aft of the vortex system, and the waves radiated forward of the

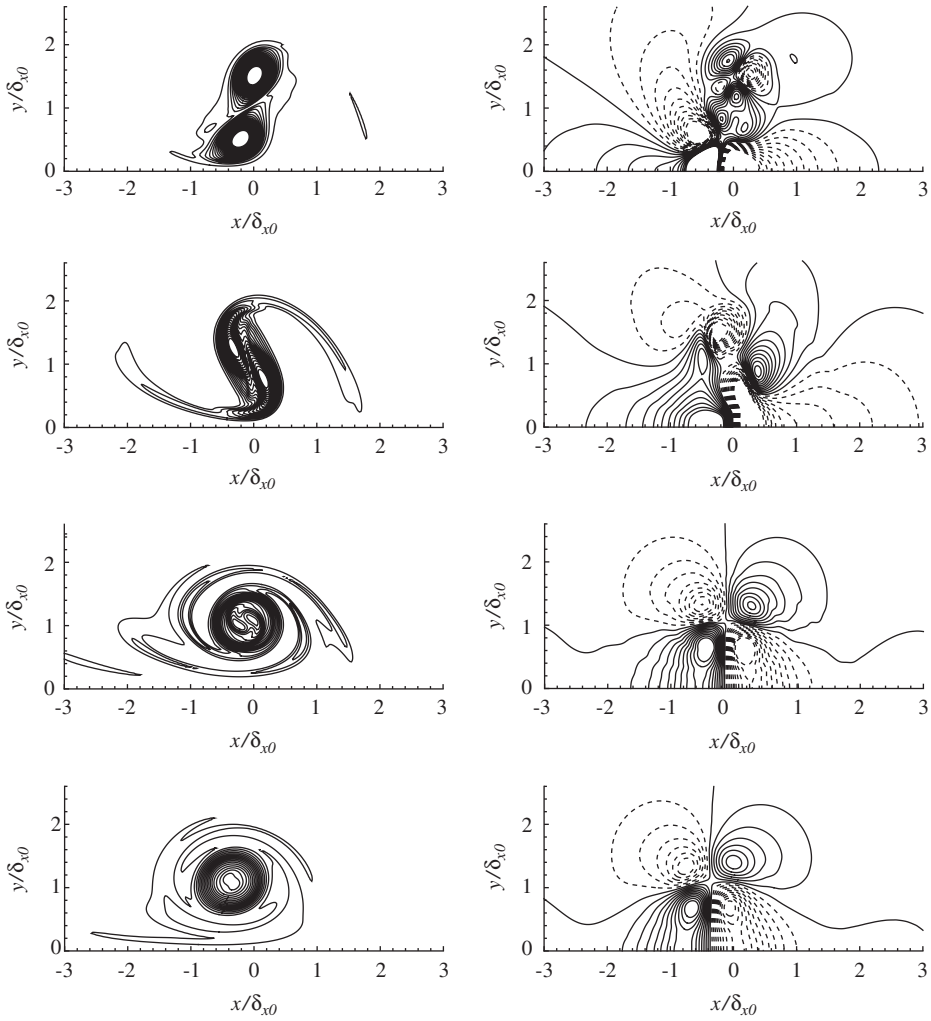

Fig. 2. (*Continued*)

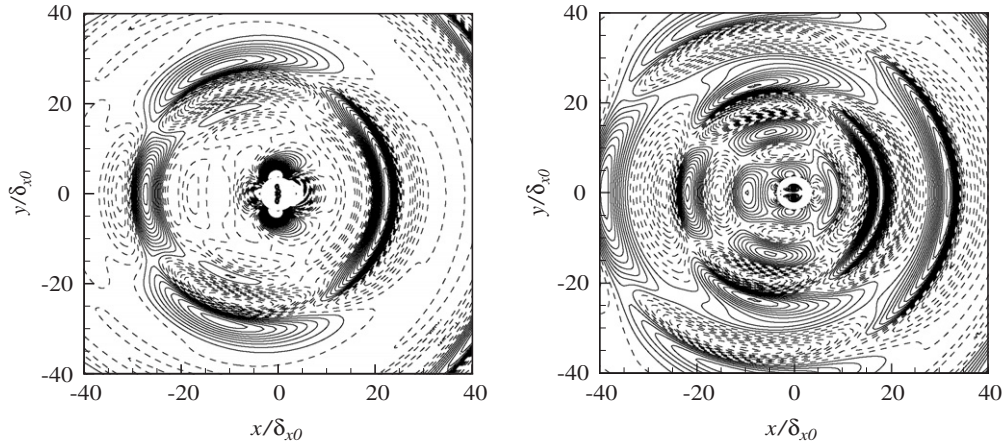

Fig. 3. Acoustic pressure field evaluated at $a_\infty t/\delta_{x0} = 110$ for vortex core sizes $r_0 = 0.25\delta_{x0}$ (left) and $0.30\delta_{x0}$ (right). Negative values are depicted with dashed lines. The Kirchhoff surface is depicted by the circle at center, along with the instantaneous vorticity field contours inside.

propagating pairs are spread over a larger sector than those emitted behind the pairs. This asymmetry is due to a Doppler effect from the mean forward motion (or equivalently, from the mean flow used to keep the vortex system stationary), and is characteristic of a convecting quadrupole. The time of travel of a wavefront, given by Eq. (A.4) in Appendix A, has an angular dependence; for a source at the origin, this travel time can be written as

$$\tau(r,\theta) = \frac{r}{a_\infty}\left[\frac{(1 - M_\infty^2 \sin^2\theta)^{1/2} - M_\infty \cos\theta}{1 - M_\infty^2}\right]. \tag{5}$$

Thus, for a wavefront of radius R, the apparent center is at $(M_\infty R, 0)$ (where $M_\infty < 0$).

The pressure field depicted in Fig. 3 for the case of the larger cores is significantly different at this instant from the previous case: the vortices are in the process of coalescing, and the acoustic field contains a greater density of wave-crests. However, the same Doppler asymmetry is apparent. The directionality of this case is made clear in Fig. 4, which depicts the rms pressure observed on a semicircle above the axis of symmetry, of radius $20\,\delta_{x0}$ and shifted center at $(20\,M_\infty\delta_{x0}, 0)$ to account for the Doppler effect. The forward lobe is larger in magnitude and angular extent than the rear lobe, and the lateral lobe is shifted slightly aft. This shift is due to the convective effect of the mean flow. The rms pressures before and after coalescence are depicted in Fig. 4. Although the magnitude of the pressure fluctuations falls significantly after the vortices coalesce, the directionality of the acoustic field does not change noticeably.

The time histories of pressure fluctuations observed at four points are depicted in Fig. 5, for the case of $r_0 = 0.30\delta_{x0}$. Each point is at a distance of $20\delta_{x0}$ from the same shifted origin used in Fig. 4. Directly ahead of the vortex pairs at 0° in Fig. 5(a), after a short time delay while the initial wavefront travels to the observer, a negative pressure peak is immediately followed by a large positive peak. This rapid pulse is the acoustic signature of the slip-through event; its duration and magnitude are not significantly different from the sound emitted by equivalent point vortices, and thus the size of the vortex cores does not strongly affect this pulse.

After the slip-through pulse, a smaller, decaying high-frequency sound is observed as the vortices undergo a relaxation toward horizontal alignment (the 'wiggles' between $a_\infty t/\delta_{x0} \approx 47$ and 60). A high-frequency component has also been observed in previous studies of this problem [8,12], but by using uniform vorticity patches these investigators observed a signal with a much larger magnitude and higher frequency, which dominated the slip-through sound and persisted without decay. Thus, the acoustic signature produced by these Gaussian-distributed cores is dramatically different from those generated by inviscid contour dynamics simulations. This aspect will be explored in Section 4.3. A second slip-through pulse of nearly identical magnitude is detected at the observation point at $a_\infty t/\delta_{x0} \approx 73$, but the subsequent relaxation period is noticeably shorter than the previous one, and the high-frequency sound is not apparent. A third slip-through pulse is rapidly followed by a fourth as the vortex cores approach each other and coalesce. After coalescence,

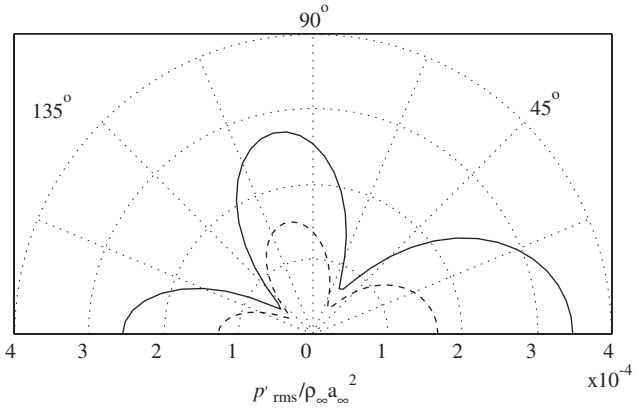

Fig. 4. Polar plots of rms pressure fluctuations before and after coalescence, evaluated at $20\delta_{x0}$ for vortex core size $r_0 = 0.30\,\delta_{x0}$. —, Pre-coalescence; - -, post-coalescence.

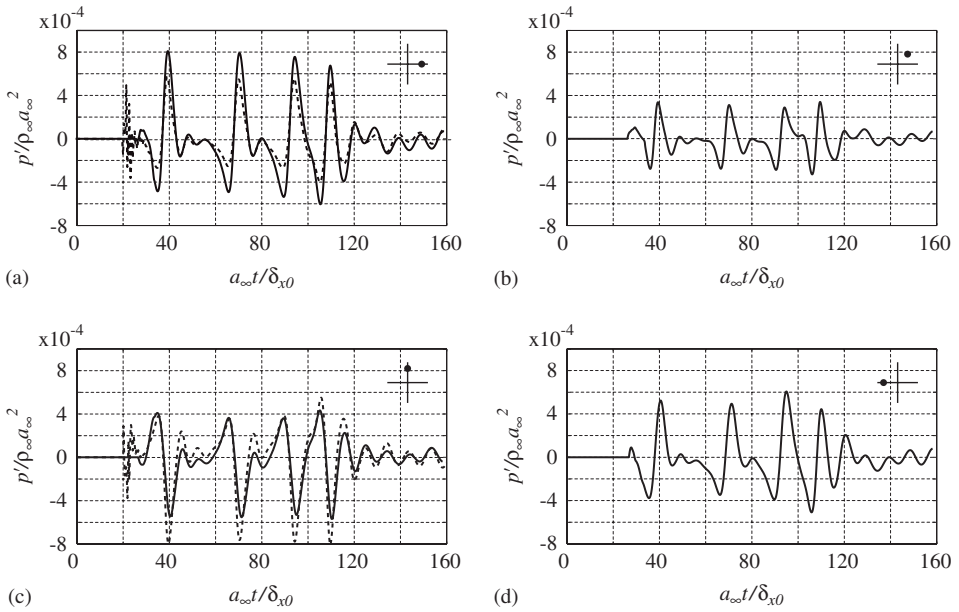

Fig. 5. Pressure fluctuations from Kirchhoff surface (—) and Möhring analogy (- -) observed at different azimuthal locations along circle of radius $20\delta_{x0}$ (relative to shifted center), for vortex core size $r_0 = 0.30\,\delta_{x0}$: (a) 0°, (b) 45°, (c) 90°, (d) 180° (angle is measured counterclockwise relative to $+x$-axis). The measurement point in each case is depicted by the inset diagram.

the measured sound suddenly changes character to small sinusoidal fluctuations, due to the relatively inefficient emissions of the single counter-rotating pair.

The acoustic signature observed at other observation points is similar in character. At 45°, which is still in the azimuthal sector corresponding to the forward lobe of the acoustic field of Fig. 5, the fluctuations are nearly identical to those at 0°, though reduced in magnitude due to the proximity of the point to the boundary between sectors. At 90°, the pressure fluctuations are of similar magnitude but opposite sign to those observed at 45°. And directly behind the vortex system at 180°, the fluctuations are similar in character to those at 0°, but weaker due to convective effects.

Eq. (1), derived by Möhring [4], identifies the third time derivatives of the second moments of vorticity as sources of sound. In the leapfrogging vortex problem, the only non-vanishing moment is $Q_1 = 2\int xy\omega\,\mathrm{d}x\,\mathrm{d}y$. The acoustic pressure computed from the two-dimensional Möhring analogy is depicted in Fig. 3 at the lateral and forward observations points. Note that, because the Möhring formula has not been corrected for convective effects, the observation points used are each at a distance of $20\delta_{x0}$ from the *unshifted* origin, in order to match the signal phases of the Kirchhoff results. In spite of the lack of Doppler correction (which would affect the sound measured forward and aft of the source), these results agree reasonably well with the acoustic signals extrapolated from the simulation with the Kirchhoff surface. The remaining discrepancy may be explained by acoustical non-compactness: though the Mach number (in this case, 0.28) is small enough to treat each co-rotating pair as an acoustically compact source, at this distance there may be non-negligible phase difference between the upper and lower pairs; indeed, at larger distances (not shown), the discrepancy in the lateral direction (where Doppler effects are absent) is reduced.

The history of the third time derivative of Q_1 is plotted in Fig. 6 for different core sizes. The noisy signal just after start-up is due to small fluctuations in the vorticity caused by passage of the initial transient. After this transient, the behavior of the source term is clearly similar in character to the pressure fluctuations of Fig. 5. In each of the first three cases, a slip-through pulse is followed in the relaxation phase by small-magnitude fluctuations of higher frequency that decay with time; in the two smallest cores, the amplitude of these small fluctuations is slightly greater after each slip-through. After coalescence, the source term changes character to nearly sinusoidal oscillations, as the sound itself does. Coalescence occurs at progressively earlier times as the

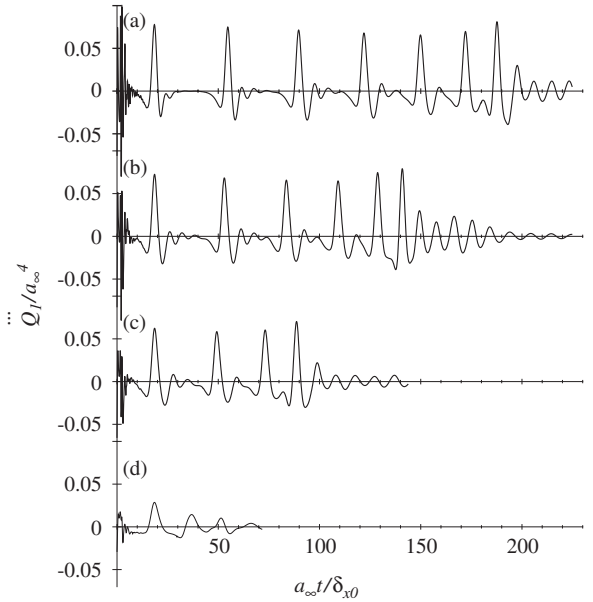

Fig. 6. Time history of Möhring source term for different initial core sizes: (a) $r_0/\delta_{x0} = 0.2$, (b) 0.25, (c) 0.3 and (d) 0.45.

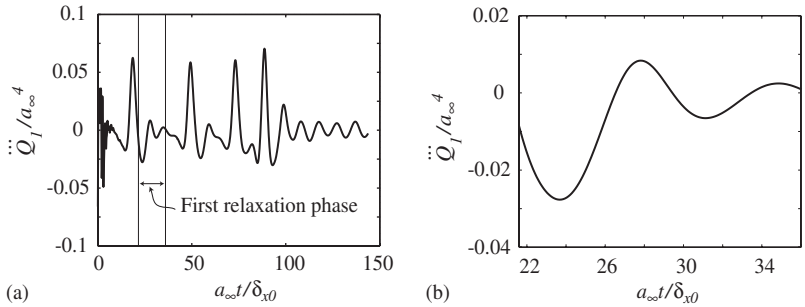

Fig. 7. Möhring source term $\ddot{Q}_1/a_\infty^4$ for case $r_0 = 0.3\,\delta_{x0}$: (a) complete time history and (b) first relaxation phase.

core thickness increases. Note that in the case of the thickest cores, $r_0 = 0.45\,\delta_{x0}$, coalescence is immediate and the source term is much weaker.

The source term for the particular case of $r_0 = 0.3\delta_{x0}$ is depicted in Fig. 7, in which the fluctuations during the relaxation phase are highlighted. These fluctuations, as shown in Fig. 7(b), resemble a decaying sinusoid, with a period of approximately $7\delta_{x0}/a_\infty$. Much of the remainder of this paper will be devoted to elucidating the connection between these fluctuations and the dynamic processes that occur in the vortex cores. In particular, the types of deformation that produce these fluctuations, as well as the reason for the decay, will be explored in Sections 4.2 and 4.3 by examining the behavior of passive tracer particles.

4.2. Dynamics

The field results presented in Fig. 2 reveal a rich dynamical behavior during the repeated processes of slip-through. Filaments of vorticity are stripped from the outer regions of each vortex as one pair passes through the other, while an inner core remains relatively intact. After a few cycles, the vortices coalesce into a single counter-rotating pair. To understand the processes occurring in the core of each vortex from a particle perspective, passive tracers are introduced and tracked, subject to the velocity field that is induced by the

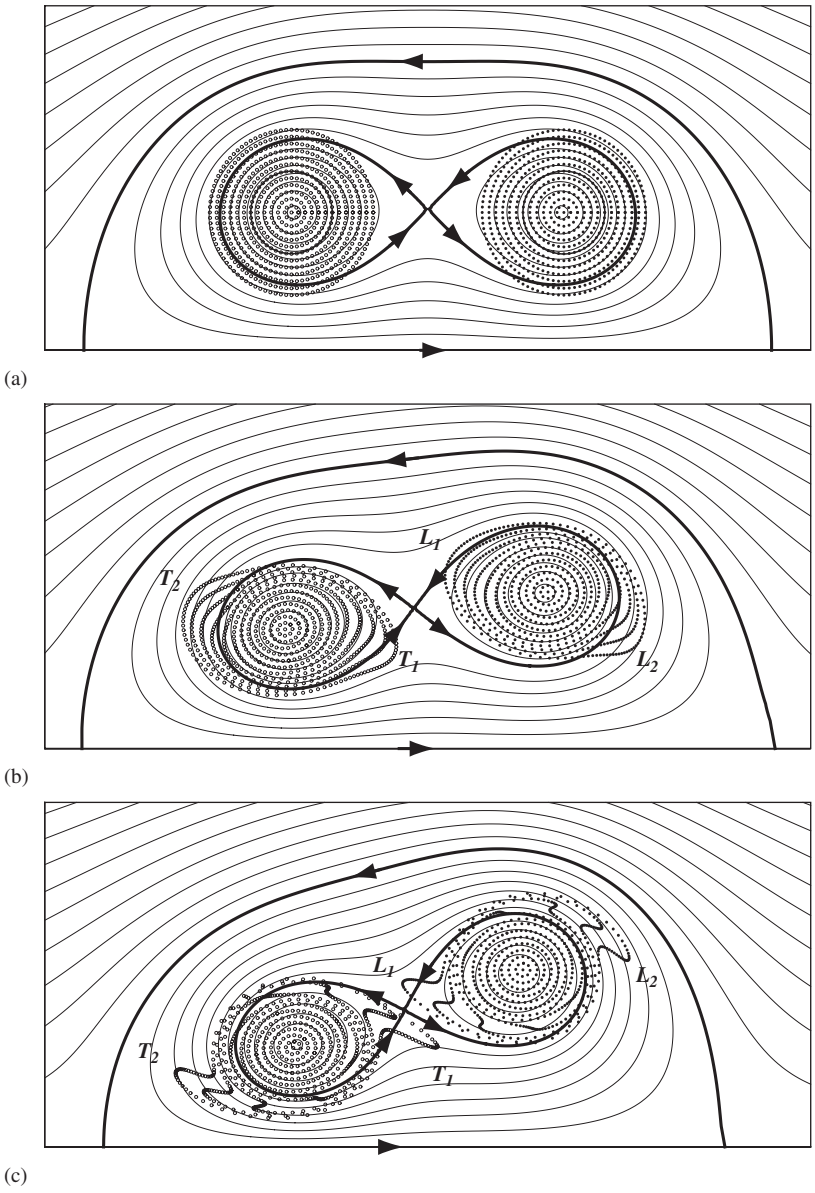

Fig. 8. Tracer particle positions and instantaneous streamlines for $r_0/\delta_{x0} = 0.3$: (a) $a_\infty t/\delta_{x0} = 0$, (b) 4.5, (c) 9.0. (d) $a_\infty t/\delta_{x0} = 13.5$, (e) 18.0, (f) 22.5. (g) $a_\infty t/\delta_{x0} = 27.0$, (h) 31.5 and (j) 36.0.

computational particles. The tracers are initially arranged about the center of each vortex core in 12 concentric rings separated by $0.05\delta_{x0}$. A predictor corrector integration scheme with a timestep size of $0.09\delta_{x0}/a_\infty$ evolve the tracer positions.

The passive tracer positions and corresponding streamlines for $r_0 = 0.3\delta_{x0}$ are depicted in the series of plots in Fig. 8, with only the upper-half plane shown. Open and filled markers are used to distinguish tracer particles that originated in the initially trailing (T) and leading (L) cores, respectively. The streamlines, evaluated in a co-moving frame, are also depicted, and are separated into distinct regions by dividing streamlines, depicted as thick lines with arrows. A figure-eight streamline separates the cores, and an outer dividing streamline—a distorted 'Kelvin oval'—encloses the system. In the initial plot, two circles inside the figure-eight streamline denote the cores of radius $r_0/\delta_{x0} = 0.3$.

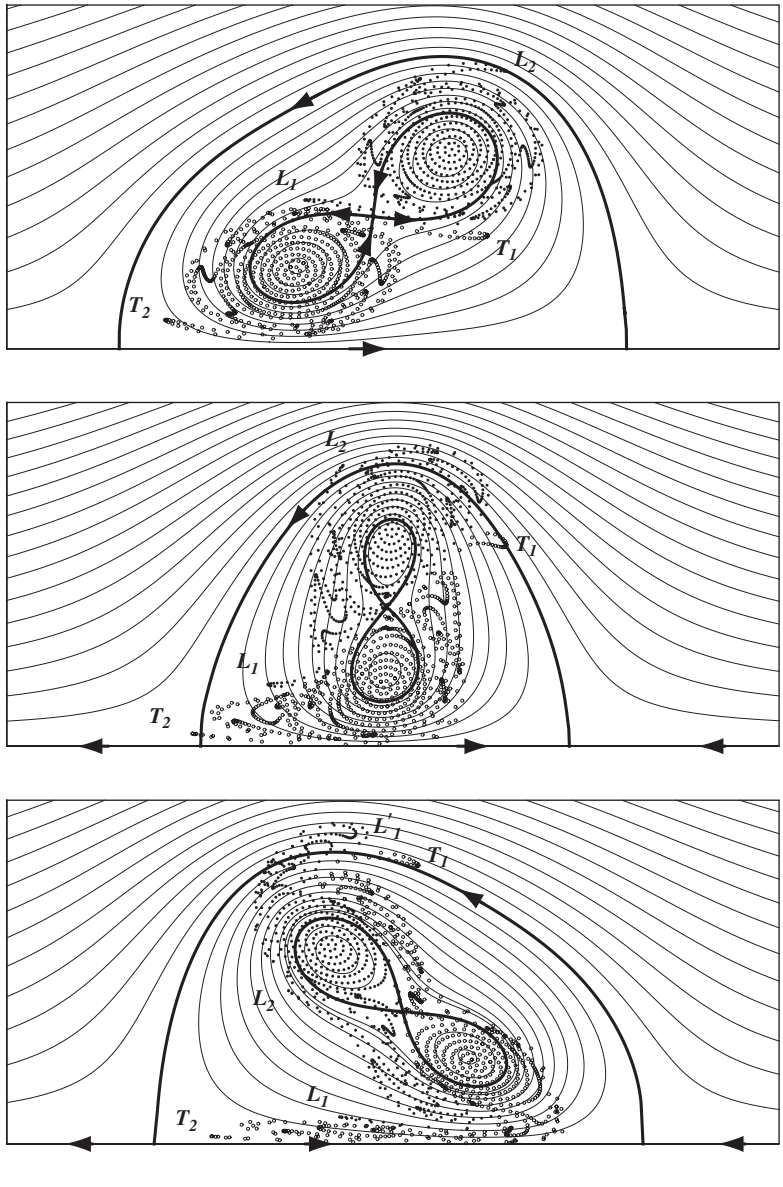

Fig. 8. (*Continued*)

For these Gaussian-distributed vortices, tracer particles in the outermost rings reveal the formation of cluster points, which sharpen and break away from the core as filaments that leak through the figure-eight streamline. The dynamics of these filaments are highly complex, as is evident by following the evolution of the labeled filaments, $L_{1,2}$ and $T_{1,2}$. After several slip-through cycles, the material exchange between the filaments facilitates the coalescence of the cores. In contrast, an inner core of tracer rings remains relatively undisturbed throughout the slip-through process. These inner core rings deform 'elastically' during the slip-through and subsequent relaxation phase, returning to nearly circular at the end of a half-cycle. Furthermore, the center of the stream-function departs sharply from the central tracer particle in each core—which also marks the center of vorticity—during the slip-through instant, and gradually re-approaches the central particle during the subsequent relaxation. (Note that when vorticity and streamfunction contours coincide in two-dimensional flow, then $\partial\omega/\partial t \approx -u \cdot \nabla\omega = 0$ and thus vorticity is nearly steady.) The distance between these two centers in

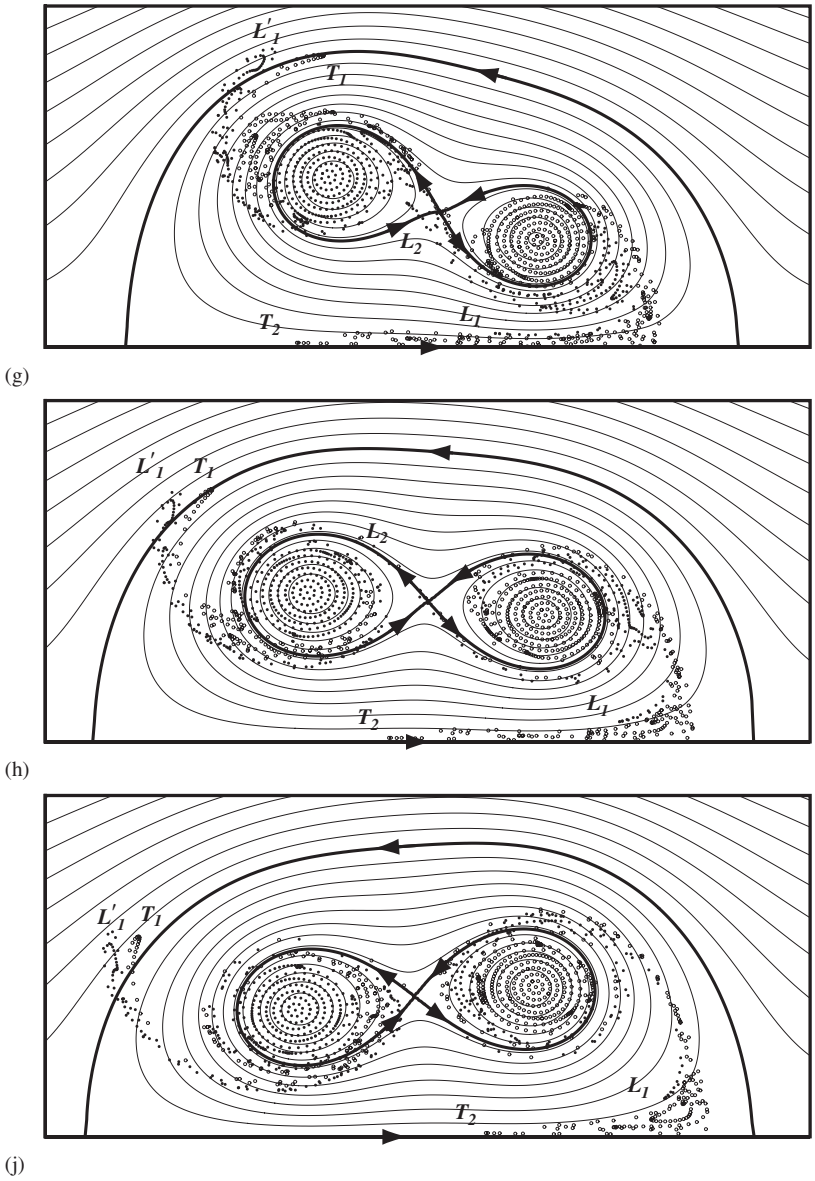

Fig. 8. (*Continued*)

each core during the relaxation phase, $a_\infty t/\delta_{x0} \in$ [21.6,36], is plotted in Fig. 9. The distance approaches a steady value of approximately $0.1\delta_{x0}$. In Section 4.3, the acoustical significance of the elastic core deformations during the relaxation will be explored.

4.3. Relation between core dynamics and acoustics

As revealed by the tracer particle plots of Fig. 8, the Gaussian-distributed vortices have an outer region from which filaments are stripped, and an inner core of approximate radius r_0 that remains intact. Previous investigations [8,11,12] have attributed the high-frequency component of the sound to the time-varying deformation of this inner core. In this section, the shapes of the material rings that are initially concentric with this core are analyzed, and their relationship with the Möhring source term (and hence the resulting sound production) is explored. It is important to note that these rings are nearly identical to vorticity contours, and

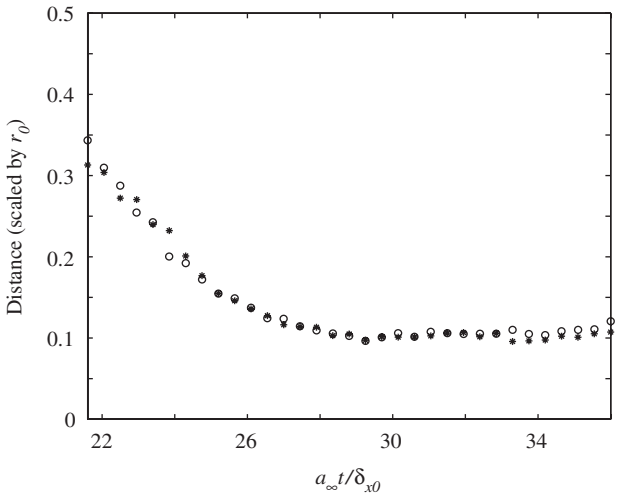

Fig. 9. Distance of tracer particle at vortex core from the corresponding center of the co-moving stream function during the first relaxation phase for case $r_0 = 0.3\,\delta_{x0}$. ○, initially leading core; *, initially trailing core.

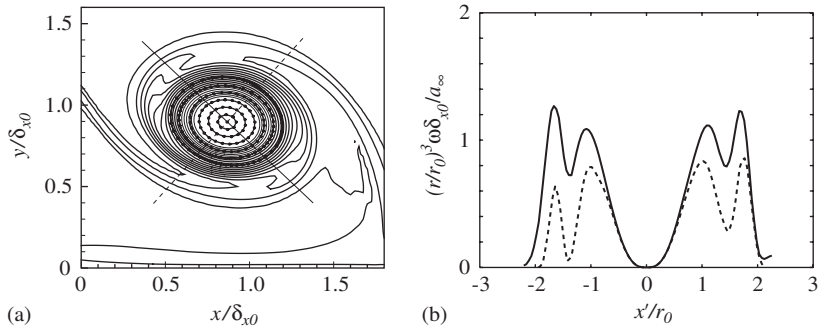

Fig. 10. (a) Vorticity contours and tracer positions for the initially trailing vortex at $a_\infty t/\delta_{x0} = 30.6$, case $r_0/\delta_{x0} = 0.3$. (b) The cross-sections of the r^3-weighted vorticity distribution corresponding to the lines shown in (a), where x' is the distance from the center, signed by x–x_0.

the central particle coincides with the point of maximum vorticity. This is apparent in Fig. 10(a), which exhibits the vorticity contours and tracer ring positions at $a_\infty t/\delta_{x0} = 30.6$, during the relaxation period following the first slip-through.

The Möhring source term involves the second moments of vorticity, and therefore polar integrals of $r^3\omega(r,\theta)\cos 2\theta$ and $r^3\omega\,(r,\theta)\sin 2\theta$, with r and θ measured relative to the core center. The r^3-weighted vorticity in the initially trailing vortex is plotted in Fig. 10(b) at $a_\infty t/\delta_{x0} = 30.6$ along two perpendicular directions. The striking feature of this plot is that two peaks are present, one at the outer boundary of the inner core, $r = r_0$, and another corresponding to the filaments that are wrapped around the core. Thus, the dynamics of the core boundary and filaments are both potentially important for sound production. Each of these features will be analyzed here. It will be shown that filamentary evolution is the primary source of the high-frequency sound observed in the figures referred to Section 4.1, whereas the core dynamics have negligible contribution.

4.3.1. Core boundary dynamics

In this section, the dynamics of the inner vortex core is analyzed using the tracer rings with initial radius less than r_0. The primary goal of this analysis is to attempt to identify the relationship, if any, between these dynamics and the acoustic signals observed in the farfield. This potential relationship is explored by comparing the frequency spectrum of the lowest modes of deformation of the ring shapes with the acoustic frequencies observed.

The shapes of these rings in the initially trailing vortex during the first relaxation period are depicted in Fig. 11. Each tracer ring is labeled by its initial radius, R_T. Its shape at subsequent times is described by the parameterized distance, $R(\theta, t)$, from the central particle, where θ is the polar angle about this particle. A Fourier series expansion of R,

$$R(\theta, t) = \bar{R} + \sum_{n=1}^{\infty} (a_n(t) \cos n\theta + b_n(t) \sin n\theta) \tag{6}$$

is used to decompose the shape of the ring. The mean radius of the ring, $\bar{R}$, remains nearly constant. However, the next higher coefficients, a_1, b_1, a_2 and b_2 (the amplitudes of the lowest deformation modes), vary significantly with time, and the frequency content of these coefficients is explored here. Note that evidence of asymmetric as well as symmetric modes is apparent in the snapshots shown in Fig. 11. In particular, asymmetry is exhibited by particles that cluster at a point in the outermost ring. Due to the hyperbolic nature of such a point, the ring bulges outward, forming the anchor point for a filament that connects the leading and trailing cores.

The power spectra of a_1 (an asymmetric mode) and a_2 (an elliptical mode) for the ring $R_T/r_0 = 1$ are shown in Fig. 12, with the spectrum of the Möhring source, Q_1, included for reference. A broad peak in both $\ddot{Q}_1$ and a_2 at the smallest frequencies corresponds to the basic leapfrogging motion. The duration of a half-cycle of this motion is approximately $36\delta_{x0}/a_\infty$ initially, so its fundamental frequency is approximately $0.028\, a_\infty/\delta_{x0}$ This frequency increases as coalescence is approached, so the peak in the power spectrum is broadened. In addition, a small peak in the Möhring source term can be distinguished at approximately $f \approx 0.14\, a_\infty/\delta_{x0}$, which corresponds to the frequency of the acoustic oscillations during the relaxation period, as shown in Fig. 7.

Notably absent from the spectrum of $\ddot{Q}_1$ (and therefore, the acoustic signal) is the large peak in a_2 that is apparent at $f \approx 0.28\, a_\infty/\delta_{x0}$. This frequency corresponds to the rate at which the ring undergoes half of one revolution, which is the dominant frequency of this elliptical (symmetric) mode. The elliptical deformation of the core boundary is therefore not a source of the high-frequency relaxation sound for these viscous Gaussian cores. This behavior contrasts dramatically from previous studies with uniform vorticity patches, in which the elliptical deformation mode produced a signal that dominated all other contributions, including the slip-through sound. Indeed, a simple elliptical model used by Shariff et al. [8] faithfully reproduced the Möhring source computed from a contour dynamics simulation.

The peak in a_1 at $f \approx 0.14\, a_\infty/\delta_{x0}$ represents the fundamental rate of ring rotation. Because this rotation rate is almost identical to the frequency of the oscillations in $\ddot{Q}_1$, it is tempting to attribute the high-frequency sound to this first deformation mode. However, as is evident in Fig. 12, the amplitude of these asymmetric

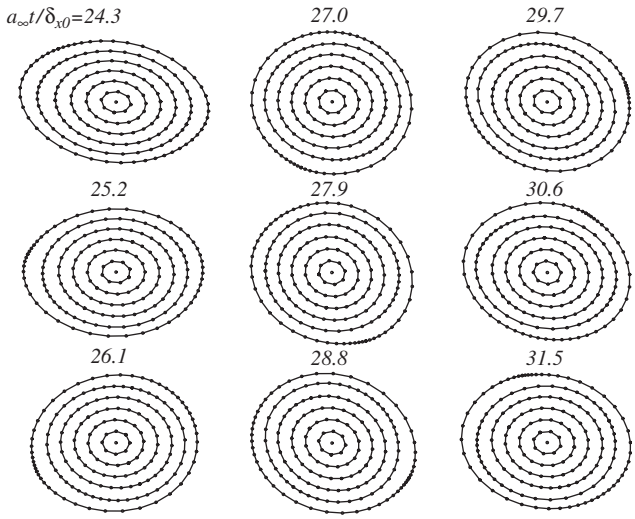

Fig. 11. Snapshots of tracer particle rings during first relaxation period in initially trailing vortex core, for $r_0/\delta_{x0} = 0.3$. The outermost ring corresponds to $R_T = r_0$.

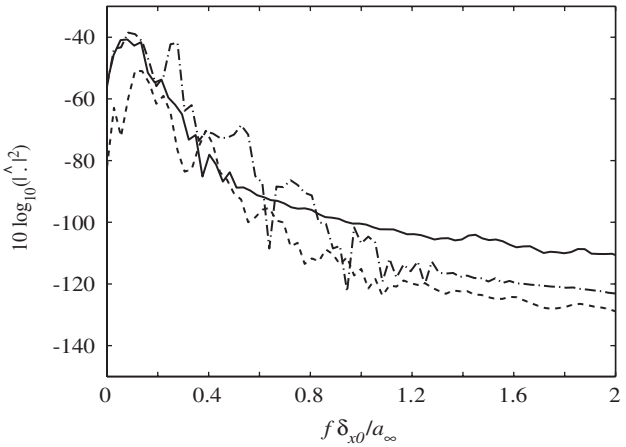

Fig. 12. Power spectra for case $r_0 = 0.3\delta_{x0}$ of $\ddot{Q}_1/a_\infty^4$ (—), and a_1 (- -) and a_2 (- · -), the first two azimuthal Fourier coefficients of tracer ring $R_T/r_0 = 1$ in initially trailing core.

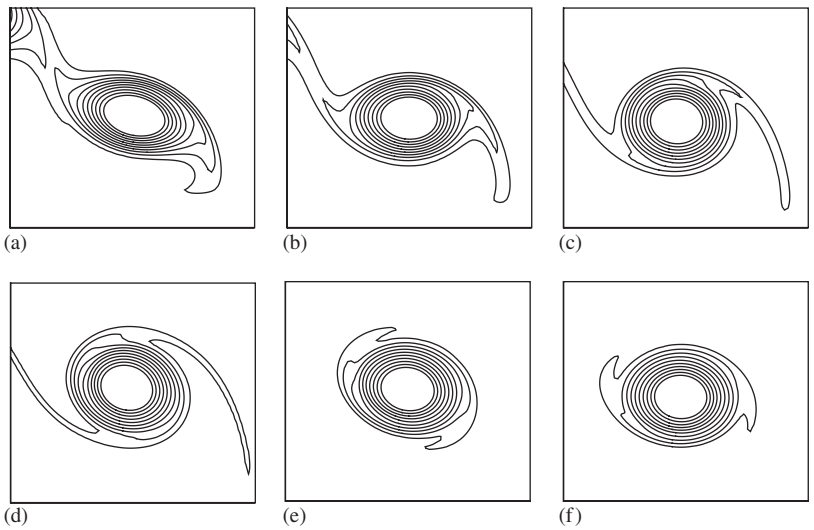

Fig. 13. Vorticity contours in the initially trailing vortex for $r_0/\delta_{x0} = 0.3$, at $a_\infty t/\delta_{x0} =$ (a) 23.4, (b) 25.2, (c) 27.0, (d) 28.8, (e) 30.6 and (f) 32.4.

oscillations is much weaker than the symmetric (a_2) oscillations, so it is unlikely that this mode would be selected in lieu of the elliptical deformation of the core.

4.3.2. Filamentary vorticity evolution

From the vorticity contours plotted in Fig. 13 at several instants during the relaxation phase, it is apparent that the deformation of the inner core is insignificant compared to the size of the filaments that are formed from its outer boundary. These filaments contribute strongly to the vorticity moment, as is evident in Fig. 10(b). The angular velocity in a Gaussian vortex at $r = 1.7r_0$, the radius of the second peak, is approximately 50% of its value at the core boundary, and thus the portions of the filaments at this radius undergo a half-rotation in the same time that the core revolves once. Indeed, a visual inspection of Fig. 13 reveals that the bases of the filaments (the hook-shaped structures) rotate a half-turn in $7.2\,\delta_{x0}/a_\infty$, which is very close to the period of the high-frequency acoustic oscillations during relaxation. The rotation of these filament anchors is the source of the oscillatory signal during this period.

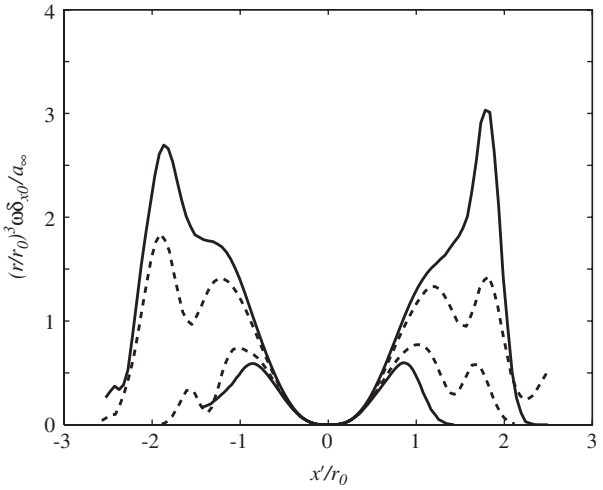

Fig. 14. The cross-sections of the r^3-weighted vorticity distribution along two lines at $a_\infty t/\delta_{x0} = 25.2$ (—) and 32.4 (- -). The larger values are evaluated along a horizontal line, and the smaller along a vertical line.

Fig. 14 depicts the cross-sections of the r^3-weighted vorticity in the initially trailing vortex at two different instants, $a_\infty t/\delta_{x0} = 25.2$ and 32.4. Referring to the corresponding vorticity contours in Figs. 13(b) and (f), the configuration of the vortex is nearly the same at both of these instants, and therefore this time interval corresponds roughly to a one-half rotation. The lines along which the vorticity is evaluated are horizontal and vertical for the larger and smaller values, respectively. It is clear that the vorticity in both filament bases has fallen after a half-cycle. During the relaxation period, the filaments are stretched and narrowed, and the diffusion is enhanced along the interface. Simultaneously, the filaments are wound around the core, which is reflected by the appearance of a new peak along the vertical direction. However, the vorticity inside the core has not changed significantly in the interval. The diffusion of vorticity along the interface of the stretching filament reduces the second moment of vorticity, and leads to the decay in the acoustic signal exhibited in Fig. 7. (It is noted in passing that simulations carried out at a Reynolds number of 10^5, though too under-resolved to be reported here, have exhibited similar initial amplitude but significantly less decay of this signal. These results reinforce the conclusion that viscous processes are responsible for damping the signal.)

5. Conclusions

In this work, the dynamics and acoustics of finite-sized leapfrogging vortex pairs have been investigated. A compressible vortex particle method, developed in previous work, has been used to solve the full compressible Navier–Stokes equations in the nearfield; the acoustic farfield has been extrapolated with a Kirchhoff method. The counter-rotating vortex pairs slip through one another, and the additional strain of the image vortices strips filaments of vorticity from each core that are subsequently stretched and diffused during the ensuing relaxation period. The development of the vortex cores and filaments during this slip-through process has been explored by tracking passive particles, revealing that an inner core remains intact at the end of each half-cycle. The leapfrogging pairs produce a rapid acoustic pulse, followed by a smaller, decaying oscillatory signal. After multiple slip-throughs, the vortex pairs coalesce into a single counter-rotating pair of elliptical vortices, and the acoustic signal becomes sinusoidal and much weaker. Throughout the entire evolution, the acoustic field is influenced by the mean forward motion of the vortex system, and exhibits the Doppler character of a convecting quadrupole.

The slip-through sound is essentially unchanged from the pulses produced by equivalent point vortices. However, the character of the high-frequency relaxation sound contrasts sharply with previous studies of finite patches of uniform vorticity. In those studies, elastic core deformation led to strong high-frequency acoustic oscillations during relaxation that were as large or larger than the slip-through pulses. In the present case with Gaussian distributed vorticity, the deformation of this inner core has been shown to be an insignificant source

of sound. Rather, it is the bases of vortex filaments that are attached to the outer core and revolve at a slower rate that produce the measured signal. As the vorticity in these filaments is diffused, the corresponding acoustic signal decays. This investigation has demonstrated the crucial importance of both initial vorticity distribution and viscous diffusion on the subsequent sound.

Acknowledgments

A preliminary version of this work was published in AIAA Paper 2005-2954.

Appendix A. Computing the far-field sound

To compute the acoustic field beyond the domain of particle coverage, a circular Kirchhoff surface is placed at a radius $R_S = R_\Omega - 0.5\delta_{x0}$. This placement is chosen to ensure that the surface is within the acoustic region of the domain, but sufficiently removed from the outer buffer zone to prevent contamination from boundary effects. The stagnation enthalpy, $B = h + |u|^2/2$, is used for the Kirchhoff extrapolation of the outer acoustic field. The two-dimensional Kirchhoff formulation, for sound propagation in the presence of a mean flow of Mach number $M_\infty = U_\infty/a_\infty$ in the x direction, can be shown as

$$B(x,t) = \frac{1}{2\pi\sqrt{1-M_\infty^2}} \int_S \int_{-\infty}^{t-\tau} \left[\frac{1}{a_\infty} \left(\frac{n_x M_\infty}{1-M_\infty^2} + \mathbf{n}\cdot\mathbf{e}_R \right) \frac{\partial B}{\partial t'} + \frac{\mathbf{n}\cdot\mathbf{e}_R}{a_\infty \Delta_+} B + M_\infty^2 n_x \frac{\partial B}{\partial x'} - \frac{\partial B}{\partial n'} \right] \frac{\mathrm{d}t'\mathrm{d}S(x')}{\Delta^{1/2}}. \tag{A.1}$$

Here, $\mathbf{n}$ is the outward normal vector on the Kirchhoff surface and $\mathbf{e}_R$ the unit directional vector from the source x' to observer x. The factor Δ is defined as

$$\Delta = \left(t - t' + \frac{M_\infty (x - x')}{a_\infty (1 - M_\infty^2)} \right)^2 - \frac{R_m^2}{a_\infty^2 (1 - M_\infty^2)^2}, \tag{A.2}$$

where R_m is a modified distance from source to observer, $R_m^2 = (x-x')^2 + (1-M_\infty^2)(y-y')^2$. This factor can be written as $\Delta = \Delta_+ \Delta_-$, where

$$\Delta_\pm = t - t' + \frac{M_\infty (x - x') \pm R_m}{a_\infty (1 - M_\infty^2)}. \tag{A.3}$$

The time integration is carried out over all times prior to the retarded time, $t-\tau$, where the travel time depends on the distance and orientation of the observation point relative to the source on the surface

$$\tau = \frac{R_m - M_\infty (x - x')}{a_\infty (1 - M_\infty^2)}. \tag{A.4}$$

It was verified that the measured acoustic field is invariant when more distant surfaces (in larger computational domains) are used.

References

[1] A. Powell, Theory of vortex sound, *Journal of the Acoustical Society of America* 36 (1) (1964) 177–195.
[2] M.S. Howe, Contributions to the theory of aerodynamic sound, with application to excess jet noise and the theory of the nute, *Journal of Fluid Mechanics* 71 (4) (1975) 625–673.
[3] S.C. Crow, Aerodynamic sound emission as a singular perturbation problem, *Studies in Applied Mathematics* 49 (1) (1970) 21–44.
[4] W. Möhring, On vortex sound at low Mach number, *Journal of Fluid Mechanics* 85 (1978) 685–691.
[5] T. Kambe, Acoustic emissions by vortex motions, *Journal of Fluid Mechanics* 173 (1986) 643–666.
[6] B.E. Mitchell, S.K. Lele, P. Moin, Direct computation of the sound from a compressible co-rotating vortex pair, *Journal of Fluid Mechanics* 285 (1995) 181–202.
[7] C. Schram, S. Taubitz, J. Anthoine, A. Hirschberg, Theoretical/empirical prediction and measurement of the sound produced by vortex pairing in a low Mach number jet, *Journal of Sound and Vibration* 281 (2005) 171–187.

[8] K. Shariff, A. Leonard, N.J. Zabusky, J.H. Ferziger, Acoustics and dynamics of coaxial interacting vortex rings, *Fluid Dynamics Research* 3 (1988) 337–343.
[9] M.V. Melander, N.J. Zabusky, A.S. Styczek, A moment model for vortex interactions of the two-dimensional Euler equations, part 1: computational validation of a Hamiltonian elliptical representation, *Journal of Fluid Mechanics* 167 (1986) 95–115.
[10] S.K. Tang, N.W.M. Ko, Basic sound generation mechanisms in inviscid vortex interactions at low Mach number, *Journal of Sound and Vibration* 262 (2003) 87–115.
[11] S.K. Tang, N.W.M. Ko, On sound generated from the interaction of two inviscid coaxial vortex rings moving in the same direction, *Journal of Sound and Vibration* 187 (1995) 287–310.
[12] S.K. Tang, N.W.M. Ko, Sound sources in the interactions of two inviscid two-dimensional vortex pairs, *Journal of Fluid Mechanics* 419 (2000) 177–201.
[13] R. Verzicco, A. lafrati, G. Riccardi, M. Fatica, Analysis of the sound generated by the pairing of two axisymmetric co-rotating vortex rings, *Journal of Sound and Vibration* 200 (1997) 347–358.
[14] O. Inoue, Sound generation by the leapfrogging between two coaxial vortex rings, *Physics of Fluids* 14 (9) (2002) 3361–3364.
[15] J.D. Eldredge, T. Colonius, A. Leonard, A vortex particle method for two-dimensional compressible flow, *Journal of Computational Physics* 179 (2002) 371–399.
[16] W. Grobli, *Special problems on the motion of rectilinear parallel vortex filaments*, Zurcher & Furrer (Zurich), 1877 (in German).
[17] W.M. Hicks, On the mutual threading of vortex rings, *Proceedings of the Royal Society of London A* 10 (1922) 111–131.
[18] G.-H. Cottet, P. Koumoutsakos, *Vortex Methods: Theory and Practice*, Cambridge University Press, Cambridge, 2000.
[19] P. Degond, S. Mas-Gallic, The weighted particle method for convection–diffusion equations, part 1: the case of an isotropic viscosity, *Mathematics of Computation* 53 (188) (1989) 485–507.
[20] J.D. Eldredge, A. Leonard, T. Colonius, A general deterministic treatment of derivatives in particle methods, *Journal of Computational Physics* 180 (2002) 686–709.
[21] B. Engquist, A. Majda, Absorbing boundary conditions for the numerical simulation of waves, *Mathematics of Computation.* 31 (139) (1977) 629–651.